Fuel 363 (2024) 130403

Contents lists available at ScienceDirect

Fuel

journal homepage: www.elsevier.com/locate/fuel

Full Length Article

Soot formation in combustion of spherically symmetric isolated fuel droplets with different initial diameters

Andrea Nobili, Alessio Frassoldati, Tiziano Faravelli, Alberto Cuoci *

CRECK Modeling Lab, Department of Chemistry, Materials, and Chemical Engineering, Politecnico di Milano, P.zza Leonardo da Vinci 32, Milano, 20133, Italy

ARTICLE INFO

Keywords:
Droplet
Microgravity
Soot
Detailed kinetics
Thermophoresis

ABSTRACT

Spherically-symmetric, isolated droplets are ideal systems to investigate the physics and the chemistry of combustion of liquid fuels. Despite their simplicity, most phenomena involved in spray combustion are still accounted for: evaporation and diffusion-induced transport, complex liquid thermodynamics, radiation, aerosol chemistry. In this work we analyzed the formation and evolution of soot particles and aggregates from the combustion of n-heptane isolated droplets. A 1D mathematical model including detailed description of thermodynamics and transport properties of liquid and gaseous phases, radiative heat transfer, and detailed homogeneous chemistry is adopted. Soot formation and evolution is described via a discrete sectional method, accounting for nucleation, surface growth, coagulation, aggregation, and oxidation.

The mathematical model was utilized in this study to investigate how the initial diameter of droplets affects their tendency to form soot. The simulations were specifically designed to examine the experimental findings of Choi et al. (2001), which indicated that droplets with intermediate diameters (~ 1.9 mm) result in the highest soot volume fraction. The numerical results reveal that this maximum is due to a competition between two phenomena: (i) increasing droplet diameter leads to a longer lifetime, thereby promoting soot formation, but (ii) larger diameters cause more radiative losses, lower flame temperatures, and subsequently, a decrease in soot formation.

1. Introduction

The combustion of liquid fuels is significant in various applications, including industrial burners, furnaces, and diesel engines, due to their high-energy density per unit volume. Typically, the combustion process of liquid fuels involves a series of stages, including atomization (spray formation), vaporization, mixing of the fuel vapors with air, ignition, flame development, and stabilization. The complex interactions among the droplets of a spray make fundamental and numerical studies of combustion of liquid fuels highly intricate. To simplify the analysis of the physical and chemical aspects of liquid fuel combustion, one strategy is to consider spherically-symmetric, isolated droplets. Despite the system's simplicity, most phenomena involved in spray combustion are still taken into account, including evaporation and diffusion-induced transport, complex liquid thermodynamics, radiation, and aerosol chemistry. In this configuration, the droplet and flame are concentric, and gas flow is entirely due to evaporation.

If soot is produced during the burning process, the soot particles and aggregates will be trapped between the droplet and the flame by a balance of the inwardly directed thermophoretic force and outwardly directed drag force due to evaporation of the fuel [1]. The resulting soot shell is a porous spherical shell-like structure. Experimental activities focused on soot formation around isolated fuel droplets were widely carried out via reduced-gravity experiments. The shell-like structure of soot, placed between the flame layer and the droplet surface, was first observed by Kumagai et al. [2]. Soot shells were also reported and discussed by several groups during the years [3–6]. In particular, the key-role of thermophoresis in the context of the soot shell was recognized for the first time by Knight and Williams [7]. More specifically, the structure of the flame enclosing the droplet was then studied by Mikami et al. [8], showing that the reaction zone is located outside of the yellow luminous zone, whose color is due to radiation from soot. The transient evolution of soot volume fraction was quantified in later works: the maximum values were found to be between 10 and 100 ppm, i.e., more than one order of magnitude higher than what observed in gas-phase diffusion flames with the same fuels [9,10].

This work analyzes the formation of soot in combustion of isolated droplets of n-heptane by means of a mathematical model, which includes detailed description of thermodynamics transport properties for both the liquid ad gaseous phases, and radiative heat transfer.

* Corresponding author.
E-mail address: alberto.cuoci@polimi.it (A. Cuoci).

https://doi.org/10.1016/j.fuel.2023.130403
Received 14 April 2023; Received in revised form 18 July 2023; Accepted 13 November 2023
Available online 17 January 2024

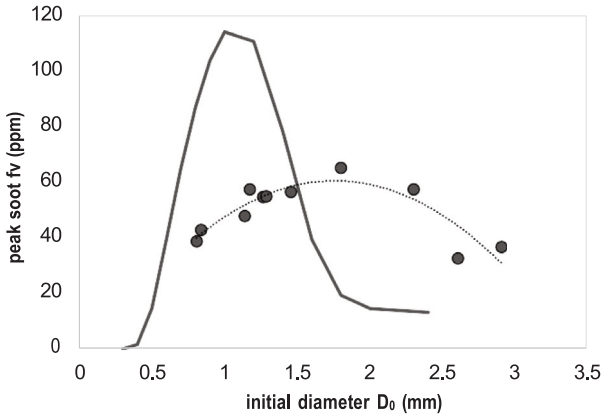

Fig. 1. Peak soot volume fraction for n-heptane droplets as a function of the initial droplet diameter D_0. Symbols are experimental points [12]. The dotted line is a curve fitting the experimental data. The solid line represents the numerical results (described in Section 4).

Combustion of n-heptane is modeled via a detailed kinetic mechanism, coupled with a Discrete Sectional Model for describing the formation and evolution of soot particles and aggregates. The adopted numerical framework is the same already adopted in Stagni et al. [11], where the emphasis was in the identification and analysis of the most relevant sub-models (thermophoresis, radiative heat transfer, etc.) to correctly describe the droplet combustion from a physical point of view. The satisfactory agreement with the experimental data (flame temperature, flame and soot shell standoff ratios, vaporization rates) demonstrated the reliability and suitability of the numerical framework to study the formation and evolution of soot from combustion of isolated n-heptane droplets.

The objective of the present paper is to explain on a numerical basis the experimental measurements of Choi et al. [12] and reported in Fig. 1. In their experiments, Choi et al. measured the peak of soot volume fraction in the combustion of isolated fuel droplet as a function of the initial diameter D_0 of the droplet. A non-monotonic behavior was observed, with a maximum of soot volume fraction for $D_0 \sim 1.9$ mm. The authors suggested a possible explanation on the basis of radiative heat transfer: increases in D_0 produce larger radiative losses (due to both soot and non-luminous components), reducing the temperatures below threshold values required for additional soot formation. In the present work we numerically investigated this hypothesis, demonstrating that the non-monotonic behavior is the result of a competition between the radiative loss (leading to lower flame temperatures) and the droplet lifetime.

The paper is organized as follows. Firstly, we provide a summary of the mathematical model adopted in this study. Next, we present and discuss the principal findings, accompanied by a comprehensive kinetic analysis of soot formation and oxidation. Lastly, we report the key conclusions of our study.

2. Mathematical model

The mathematical model (already presented and discussed in [13]) describes the combustion of an isolated fuel droplet in a gas-phase environment, in 1D spherical-symmetric conditions. The main following assumptions are taken into account: (i) spherical symmetry and absence of natural convection effects; (ii) constant pressure; (iii) no reactions in liquid phase; (iv) thermodynamic equilibrium at the liquid/gas interface. The conventional transport equations for total mass, energy, and species are included for both the liquid and the gaseous phase, together with proper boundary and initial conditions. The complete set of equations is provided in the Supplementary Material (SM). Here below we provide some details about the modeling of thermophoresis and radiative heat transfer, playing a key-role in soot formation around isolated fuel droplets.

2.1. Thermophoretic effect

The thermophoretic effect on carbonaceous particles produced by the combustion process is included in the model. The thermophoretic velocity v_{th} is given by the following expression [14]:

$$v_{th} = -V_{th,r}\frac{\mu_G}{\rho_G}\frac{\nabla T_G}{T_G} \quad (1)$$

where μ_G is the dynamic viscosity, ρ_G the density, T_G the temperature, and $V_{th,r}$ the thermophoretic diffusivity (or reduced thermophoretic velocity). Stagni et al. [11] provided an extensive discussion about the estimation of such thermophoretic diffusion and compared different theoretical model and assumptions. The description is particularly complex, because thermophoretic velocities depend on primary particle sizes (related to the open structure of the aggregates). In the present work, $V_{th,r} = 0.654$ is assumed.

2.2. Radiation

The transport equation for energy in the gaseous phase accounts for the radiation contributions from non-luminous gases (mainly CO_2 and H_2O) and luminous soot particles. Different approaches, with different levels of accuracy and complexity, are available in the adopted code to model the radiative heat transfer: the optically-thin model, the analytical solution proposed by Viskanta and Merriam [15], the P1 radiation model, and the Discrete Ordinates Model (DOM) [16]. In the present work we adopted the P1 model, which represents a good compromise between computational load and accuracy.

2.3. Boundary and initial conditions

Symmetry conditions are imposed in the center of the droplet $r = 0$. At the outer boundary $r = R_\infty$ (with R_∞ ~100 times the initial droplet radius), Neumann's boundary conditions are adopted. To enforce the ignition, a temperature profile peaking at ~2200–2400 K is imposed as initial condition in the proximity of the liquid interface. Additional details are reported in the SM, to demonstrate that the droplet and soot evolution are only marginally affected by the ignition procedure. Although in experimental devices the spark- or hot-wire-ignition might in principle compromise the spherical symmetry, this effect is neglected in this model, as already done in previous works [13,17].

2.4. Numerical solution

The overall model consists of a system of partial differential equations for the liquid and gaseous phases. The two sets of equations share the liquid/gas droplet surface, where proper interface conditions are prescribed. Boundary conditions are defined at the droplet center and at the outer radius of the gaseous phase surrounding the droplet. The partial differential equations are numerically solved through the method of lines, which consists in discretizing the spatial derivatives only, leaving the time variable continuous. In particular, the spatial discretization, based on the Finite Difference Method (FDM), is applied on a 1D moving spatial mesh. The convective terms appearing in the governing equations are discretized using the first-order upwind discretization for stability reasons, while the second-order derivatives associated to the conduction/diffusion terms are discretized using a second-order centered scheme. After spatial discretization, the original problem is transformed into a DAE (Differential–Algebraic Equations) system, i.e., a set of differential equations in time and algebraic equations corresponding to boundary conditions and liquid/gas interface conditions. Such a DAE system is solved by a specifically conceived DAE solver for stiff problems, which exploits the block-tridiagonal structure of the associated Jacobian matrix. The DAE solver is based on the BDF technique [18] and it is derived from the `BzzDae` solver [19,20]. Sensitivity analyses were carried out to test the independence of the solution to the number of grid points. Additional details are available in the SM.

3. Kinetic model

The kinetic model adopted consists of 226 species and 10358 reactions, coupling gas-phase [21] and soot [22] chemistry. Specifically, the soot sub-model is developed through a discrete sectional approach. Heavy PAHs and soot particles are discretized into 25 sections of lumped pseudo species, called BINs, from 20 to $3 \cdot 10^8$ C-atoms, with a spacing factor of two between the number of C-atoms of adjacent sections. BIN1-4 represent large PAHs, while BIN5, with 320 C-atoms ($D_p \sim 2$ nm), is the smallest soot particle. Soot particles from BIN5 to BIN12 are considered spherical. BIN12, with $4 \cdot 10^4$ C-atoms ($D_p \sim 10$ nm), is selected as the primary particle, i.e., the building block of soot aggregates. An increasing density from nascent to mature soot, i.e., from 1.1 g/cm^3 for BIN5 to 1.85 g/cm^3 for BIN25 ($D_p \sim 190$ nm), is also implemented. Furthermore, three hydrogenation levels (A, B, C) are considered for each BIN to account for dehydrogenation and aging processes [22]. Based on both experimental [23,24] and theoretical [25] evidence, large gas-phase and solid aromatic structures from BIN4 (160 C-atoms) are considered persistent radicals and they are not distinguished from their closed-shell counterparts, thus allowing to strongly reduce the number of soot species included in the kinetic model. Detailed information about the soot model and its validation can be found in previous studies [26,27].

4. Results and discussion

According to the classical theory of isolated droplet evaporation and combustion, the vaporization rate K of isolated droplets is predicted to be constant and independent of time and initial droplet diameter D_0 [28]. However, experiments carried out in microgravity conditions on large droplets show that K decreases as D_0 increases, with possible additional dependency on time [10]. Scale analyses [1] and numerical simulations [17,29] demonstrated that this phenomenon is explained by the increasing radiative heat loss from the flame with increasing D_0, leading to a significant decrease of flame temperature T_f, which produces a decrease in the vaporization rate K. The numerical simulations carried out on pure n-heptane droplets confirm the experimental observations and identify three vaporization regimes based on D_0, as depicted in Fig. 2 (continuous lines):

1. Regime I (diffusive regime): for sufficiently small droplet diameters ($D_0 < 0.6$ mm), the vaporization rate K and the flame temperature T_f are independent of D_0 (in agreement with the theory);
2. Regime II (intermediate regime): for intermediate D_0 values ($0.6 < D_0 < 2.2$ mm), the vaporization rate K decreases with increasing D_0, mainly because of the increasing role of heat loss from the flame, which produces a significant decrease of flame temperature T_f;
3. Regime III (radiative-extinction regime): for large D_0 values ($D_0 > 2.2$ mm), radiative losses from the flame to the environment becomes dominant over diffusive transport, leading to the extinction of the flame. In some cases, a transition to low temperature combustion (LTC) or cool flames regime (not considered in the present work) has been observed [17,30].

Simulations carried out without considering radiative heat transfer (Fig. 2, dashed lines) show that the vaporization rate K is independent of D_0, in agreement with theoretical expectations.

Fig. 3 shows the temporal evolution of squared droplet diameter D^2 and flame stand-off ratio (D_f/D, where D_f is the diameter corresponding to T_f and D is the current droplet diameter) for droplets with different initial diameters, selected in the three different vaporization regimes. The largest droplet ($D_0 = 2.4$ mm) shows a radiative extinction, which is easily identified by the change of slope of D^2 curve and the disappearance of the flame. Even if the flame extinguished, vaporization still takes place because of the high temperature of the droplet. The numerical prediction of radiative extinction is usually very sensitive to the radiative heat transfer and the optical properties of the gaseous environment. No additional investigations were carried out here, because of marginal relevance of these aspects to the purposes of this work. More details can be found in [11].

As explained and numerically demonstrated by Stagni et al. [11] (Fig. 9), if soot is produced during the burning process, the soot particles are trapped in the region between the droplet surface and flame front (i.e., where the maximum temperature occurs), as a result of the competition between the convective flow generated by fuel evaporation (Stefan flow) and thermophoresis, due to the large temperature gradients close to the droplet surface. Indeed, soot particles are exposed to both the convective velocity directed outwardly and the thermophoretic velocity, which is directed inwardly (diffusion velocity can be assumed to be negligible). Accumulation occurs where the net velocity experienced by the particles is null. Fig. 4 shows the calculated spatial profiles of temperature and soot volume fractions at several times for a $D_0 = 1$ mm droplet: the thickness of the sooting region decreases in time, but the peak of soot volume fraction continuously increases, leading to the formation of a soot shell, in agreement with experimental observations.

Fig. 1 shows the peak soot volume fraction predicted by the simulations as a function of the initial droplet diameter D_0, compared with the experimental data introduced at the beginning of this work. Even if the numerical simulations confirm the non-monotonic behavior, the quantitative agreement with the experimental data is not completely satisfactory. The maximum soot volume fraction is overestimated by a factor of ~ 2 and the predicted maximum location occurs at ~ 1 mm, while the experimental maximum is located at ~ 2 mm. However, despite these discrepancies, the numerical results are valuable, since they are able to capture experimental trend, which is the main purpose of the present work. In evaluating the quality of the numerical results, it is important to keep in mind some points:

1. The system under investigation is extremely complex from the physical and chemical point of view, including multiple phases, evaporation, radiation and homogeneous and heterogeneous reactions. Simplifications and assumptions in the description of some phenomena are unavoidable (for example, spherical symmetry, ignition process, soot model), which may introduce deviations from the experimental data.
2. Due to the complexity of the system, it is reasonable to imagine that experimental measurements are also affected by errors (unfortunately not reported in [12]).
3. No *ad hoc* tuning of individual sub-models was considered in the present work. In principle, there is room to improve the agreement with the experimental data, especially working on more advanced radiative heat transfer model.

By combining the observations and the analyses reported above, the experimental trend can be explained on the basis of a competition between the time available for soot formation (i.e., the droplet life-time, t_{life}) and the chemical time t_{chem} governing the soot formation. More specifically, the droplet life-time t_{life} increases with the initial diameter according to $t \sim D_0^2$ (page 34 of [28]). The characteristic chemical time can be written as the inverse of a pseudo-first-order kinetic constant, which is a function of the flame temperature T_f according to the Arrhenius' law:

$$t_{chem} \sim \frac{1}{k_{soot}} \sim e^{\frac{E}{RT_f}} \tag{2}$$

where a global activation energy $E = 30$ kcal/mol, based on [22], is assumed for the soot formation process.

By looking at the flame temperature reported in Fig. 2, it is clear that t_{chem} increases with the droplet diameter D_0, since the flame temperature T_f decreases. Thus, both t_{life} and t_{chem} increase with D_0,

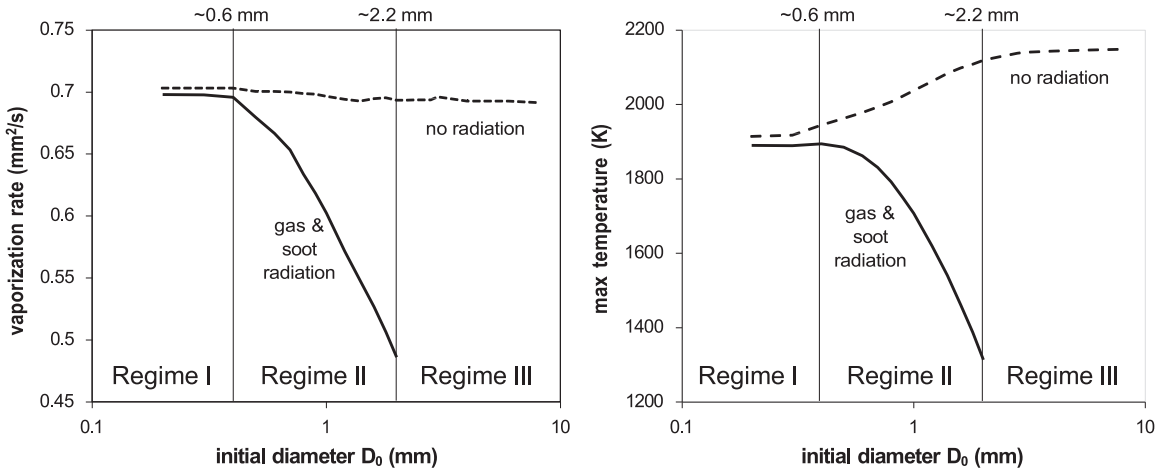

Fig. 2. Vaporization regimes in combustion of isolated fuel droplets of pure n-heptane. Left panel: Average vaporization rate K as a function of D_0; Right panel: Flame temperature T_f (defined as the maximum temperature in the gaseous phase during the quasi-steady vaporization stage) as a function of D_0.

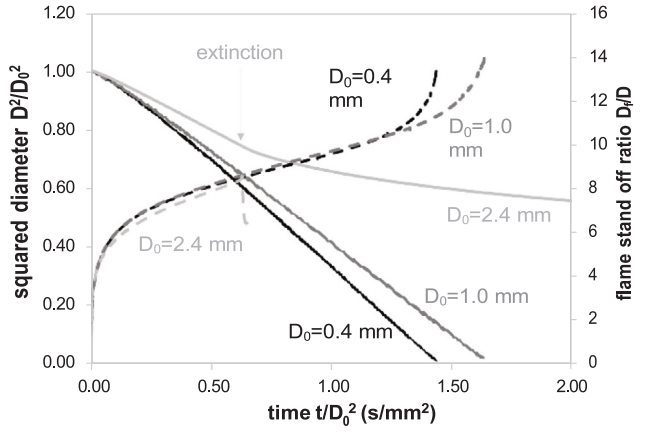

Fig. 3. Temporal evolution of squared droplet diameter D^2 and flame standoff ratio D_f/D for droplets with different initial diameters.

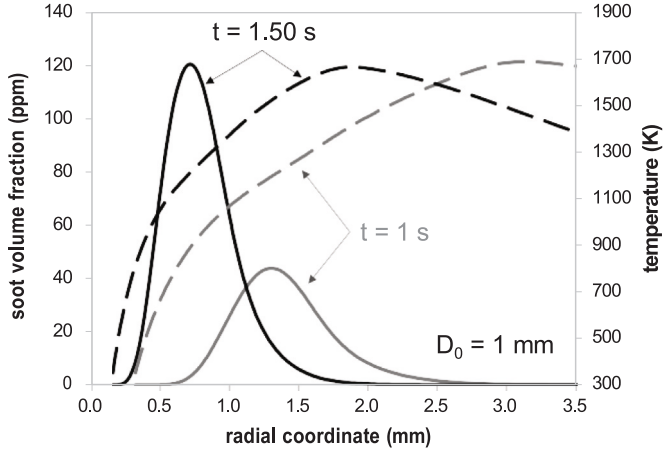

Fig. 4. Radial profiles of soot volume fraction and temperature for a n-heptane droplet of initial diameter of 1 mm at times t=1.0 s and t=1.5 s. Continuous lines: soot volume fraction; dashed lines: temperature.

but with different rates. The result is that their ratio has a maximum, as reported in Fig. 5. More specifically, the maximum is located at $D_0 \sim 1$ mm, which is approximately the diameter size at which the

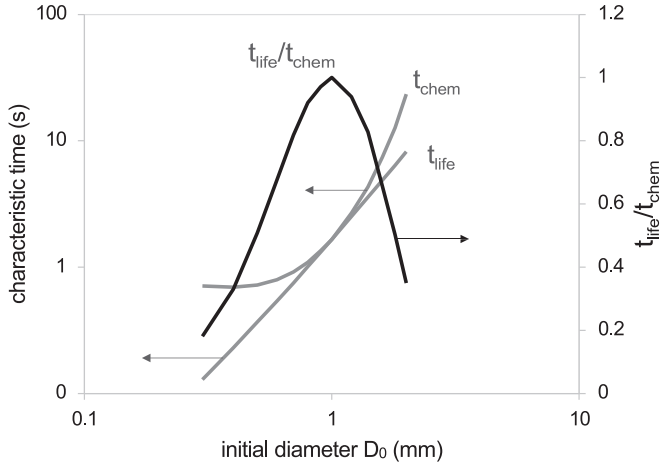

Fig. 5. Comparison of characteristic times to explain the non-monotonic behavior of soot volume fraction as a function of the initial diameter. The characteristic times are evaluated by an order of magnitude analysis.

numerical simulations predicted the maximum of soot volume fraction (see Fig. 1).

Additional simulations were performed without considering the radiative heat transfer (from both gaseous phase and soot particles and aggregates). Without the inclusion of radiative heat transfer, the soot production increases exponentially with the droplet diameter (mainly because of the larger flame temperatures coupled with), reaching local mass fractions close to ~ 1. More specifically, the model is not able to return a solution for droplets larger than ~ 1.2 mm. In fact, the modeling assumptions at the basis of the adopted numerical framework (according to which the soot sections, i.e. the BINs, are treated as gaseous pseudo-species) are not compatible with such large soot production. However, in our opinion, the unrealistic soot volume fractions obtained without radiation further suggest that the experimentally observed non-monotonic behavior is the result of the competition between radiation and droplet lifetime. More details can be found in the SM.

The numerical results were investigated to further support the proposed explanation, based on the competition of characteristic times. Fig. 6a shows the temporal evolution of peak soot volume fraction f_v^{max} and flame temperature T_f for droplets with initial diameters of 0.6, 1 and 2.4 mm. As discussed before, because of radiative heat loss, the flame temperature decreases with increasing D_0 and this easily explains why f_v^{max} for the larger droplet ($D_0 = 2.4$ mm) is so small. The

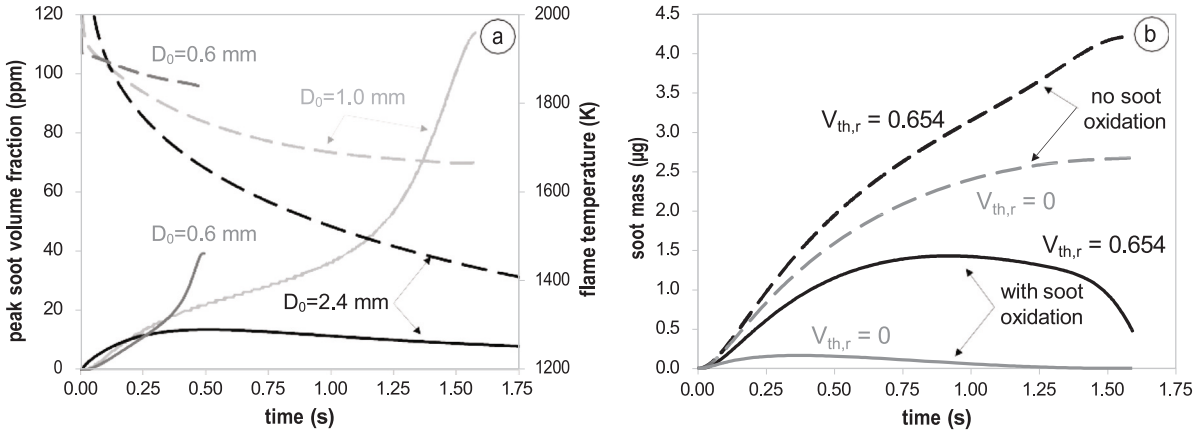

Fig. 6. (a) Temporal evolution of peak soot volume fraction fv_{max} (continuous lines) and flame temperature T_f (dashed lines) for droplets with initial diameters of 0.6, 1.0 and 2.4 mm. (b) Temporal evolution of total mass of soot for a droplet with initial diameter of 1 mm. Dashed lines refer to results without including oxidation of soot. $V_{th,r}$ is the thermophoretic constant appearing in Eq. (1).

smaller droplet shows a strong tendency to soot formation, apparent from the sudden increase in f_v^{max} and mainly due to the larger flame temperature, but is unable to reach the same level of soot volume fraction (120 ppm) experienced by the intermediate droplet (D_0 = 1.0 mm) simply because its life-time is too short.

As demonstrated in previous works, thermophoresis plays a major role in determining the position of the soot shell, leading to soot concentrations which are usually never reached in conventional combustion systems, like premixed or counter-flow diffusion flames. Fig. 6b shows the temporal evolution of soot mass in the gaseous phase for the 1 mm droplet when the thermophoretic velocity is included or not in the numerical simulation. The impact is very strong: without the thermophoretic velocity, the total amount of soot decreases by more than one order of magnitude and basically no soot shell formation can be observed. Simulations carried out by removing soot oxidation show a different behavior: the produced mass of soot is very similar in both cases, i.e. with or without inclusion of thermophoresis. This suggests that without thermophoresis, soot production still occurs, but soot particles and aggregates are transported by the convective flow towards the flame front, where most of them are oxidized. Thus, accumulation of soot is not possible and no formation of soot shell can occur. On the contrary, the thermophoretic velocity pushes the soot particles and aggregates towards the droplet surface, against the convective flow, preventing (or limiting) their oxidation. This is especially evident through the comparison of Figs. 6a and 6b: even if the total amount of soot starts decreasing at $t \sim 1.0$ s, the corresponding soot peak volume fraction fv_{max} continues to increase, even more rapidly, which indicates that soot particles are pushed by the thermophoretic velocity in a region which is thinner and thinner (which is the soot shell).

4.1. Kinetic analysis

Kinetic analysis allows to depict the chemical evolution of large gas-phase polycyclic hydrocarbons (PAHs) towards soot spherical particles and aggregates varying the initial diameter of n-heptane droplets.

Fig. 7 reports the large PAH mole fraction, the particle number density and the soot volume fraction fields for n-heptane droplets with initial diameter of 0.6 mm (Fig. 7a), i.e. at the border of regimes I and II (Fig. 2), 1.0 mm (Fig. 7b), where the highest PAH and soot concentrations are reached, and 2.0 mm (Fig. 7c), i.e. at the border of regimes II and III (Fig. 2). For all the three droplets, large PAHs rapidly produced from fuel evaporation and combustion (left panels in Figs. 7a-c), evolve to spherical particles, which primarily contribute to the overall particle number density [31] (middle panels in Figs. 7a-c), and finally to larger aggregates (up to ~ 200 nm), which accumulate and govern the final soot volume fraction. Fig. 7 also shows that while large PAHs concentrate close to the flame sheet, spherical particles and then aggregates reach their highest concentrations along the soot shell, being convected inwardly by thermophoresis. Moving from small (D_0 = 0.6 mm) to large (D_0 = 2.0 mm) droplets, large PAH- and soot particle-dense regions shrink, while the temporal increase of soot volume fraction on the soot shell is more pronounced for the D_0 = 1.0 mm droplet, i.e. the one with the highest sooting tendency.

Fig. 8 shows the relative contribution of each lumped pseudo species considered in the soot model for spherical particles (BIN5-12) and aggregates (BIN13-25) to number density at t = 0.3 s and to volume fraction at t = 0.5 s for the n-heptane droplet with D_0 = 1.0 mm. It highlights the dominant contribution of spherical particles to the maximum number density and the one of aggregates to the peak soot volume fraction.

Moreover, the evolution over time of the soot particle size distribution function (PSDF) on the soot shell (dashed line in Fig. 7b) for the n-heptane droplet of initial diameter of 1 mm is reported in Fig. 9. At t = 0.1 s, the PSDF is quasi-unimodal and constituted by spherical particles (BIN5-12, $D_p < 10$ mm). As soot inception and surface growth proceed, the number density of spherical particles increases, and the first soot aggregates start forming at t = 0.5 s. The transition from unimodal to bimodal PSDF, also typically observed in laminar premixed flames [32], becomes evident at t = 1.0 s, when the contribution of coalescence and aggregation prevails. Finally, at t = 1.5 s, only soot aggregates (BIN-13-25, see Fig. 8) are present close to the soot shell and the tail of spherical particles completely disappears.

Different reaction classes govern soot formation and growth from gas-phase PAHs, i.e. the soot precursors. Temporal evolution of the integral, net formation rates of large PAHs, soot spherical particles and aggregates, and of the rates of the main reaction classes included in the soot model [22] are reported in Fig. 10 for the D_0 = 1.0 mm droplet. Qualitatively analogous profiles characterize the droplets with initial diameters of 0.6 mm and 2.0 mm. Large PAHs form in the early life-time of the droplet and grow through inception mechanisms up to 4 ms (I in Fig. 10a), despite concurrent oxidation (Fig. 10b), leading to the first soot nuclei. Then, spherical particles growth becomes dominant up to 13 ms (II in Figs. 10a and 10c) until coalescence towards aggregates occurs. Due to a related steep increase in growth reactions (Fig. 10c), at 20 ms the net formation rate of spherical particles starts increasing again (mainly through PAH radical condensation reactions [22]) up to a second peak at 30 ms (III and IV in Fig. 10a, respectively), when instead coalescence and agglomeration prevail. Aggregate growth becomes dominant, leading to the peak in the aggregate net formation rate at 100 ms (V in Fig. 10a). From here on, aggregate formation decreases due to both temperature reduction (Fig. 6) and oxidation (Fig. 10c), the latter becoming dominant in the final droplet life-time (VI in

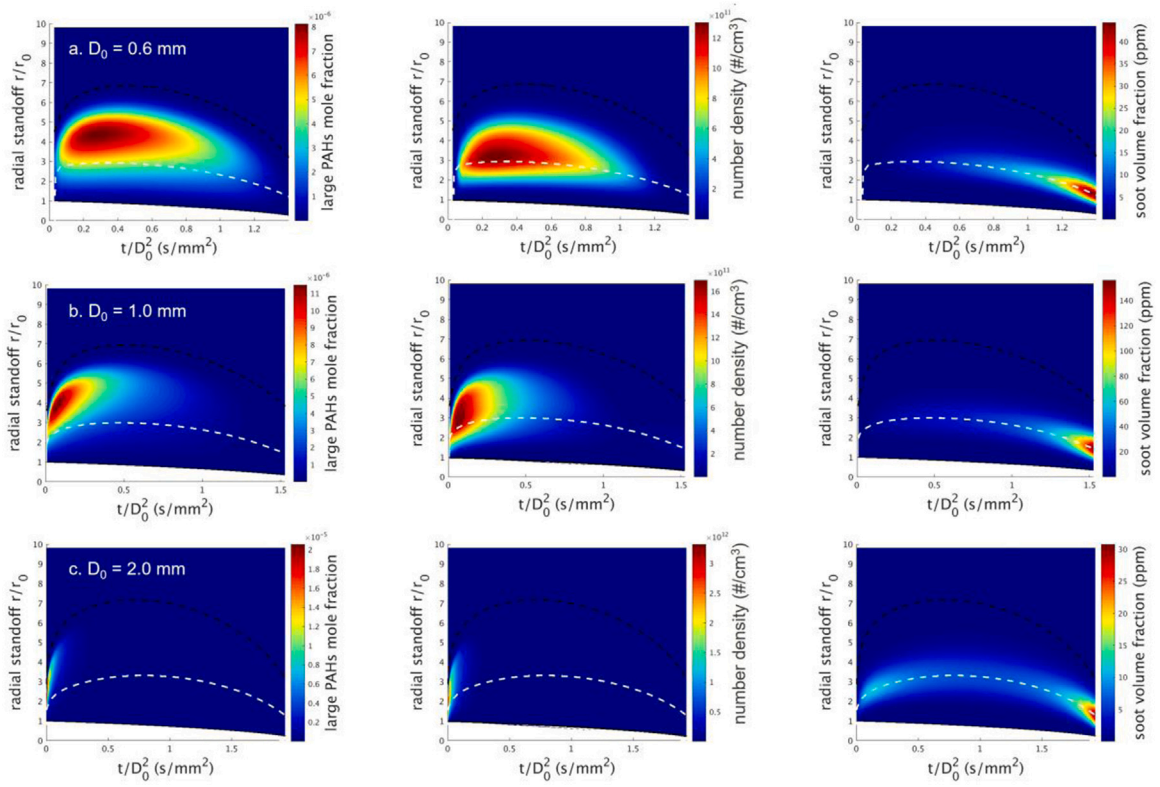

Fig. 7. Large PAH mole fraction (left panel), particle number density (middle panel) and soot volume fraction (right panel) fields for n-heptane droplets with different initial diameters: (a) 0.6 mm; (b) 1.0 mm; and (c) 2.0 mm. Dashed black and white lines indicate the location of the flame sheet and the soot shell, respectively.

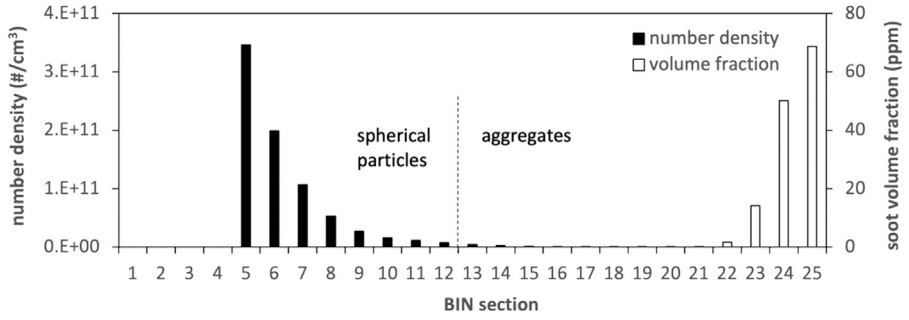

Fig. 8. Contribution to maximum number density (at t = 0.3 s) and to peak soot volume fraction (at t = 1.5 s) of the different lumped pseudo species (BINs) adopted in the kinetic model to describe soot particles and aggregates (BIN13-25) for the n-heptane droplet with D_0 = 1.0 mm.

Fig. 10a), leading to the corresponding soot mass reduction shown in 6b. HACA (Hydrogen Abstraction Carbon Addition) mechanism, spherical particle oxidation and dehydrogenation are also reported in Fig. 10c, but their contribution to the global soot concentration is limited. The role of HACA mechanism in the soot chemistry was discussed by Pejpichestakul et al. [27], who showed that acetylene prompts soot growth indirectly, through addition to the most abundant PAHs, rather than through direct addition to the heavy aggregates present in lower concentrations.

The spatial profiles of the main soot reaction classes in a n-heptane droplet were analyzed in a previous work [11]. Here, radial profiles of maximum flame temperature and peak soot volume fraction for D_0 = 1.0 mm droplet reported in Fig. 6 are extended to D_0 = 0.6 mm and D_0 = 2.0 mm droplets for different times (t = 0.1, 0.5 and 1 s) in Fig. 11a and Fig. 11b, respectively, to further highlight the main differences on soot evolution varying the droplet initial diameter. Radially integrated rates of the main soot reaction classes at t/D_0^2 = 0.1 and 0.5 s/mm^2 (11c) and radial profiles of net velocity (Fig. 11d) are also reported. Independently of D_0, the maximum flame temperature decreases with time (Fig. 11a). However, from t = 0.1 s to t = 0.5 s the temperature in the soot formation region (strongly shifted closer to the flame sheet with respect to the soot-dense region due to thermophoresis [11]) remains high allowing soot volume fraction to continuously increase (Fig. 11b). At t = 1 s, instead, the sooting tendency of the three droplets is completely different. The D_0 = 0.6 mm droplet is already completed consumed (at t 0.5 s in Fig. 6) so that soot cannot be further produced; on the other hand, soot volume fraction further increases for D_0 = 1.0 mm thanks to the still high temperature (T > 1500 K) in the soot formation region, conversely for D_0 = 2.0 mm it decreases due to the low temperature which prevents soot growth but not oxidation [33]. Indeed, as shown in Fig. 11c, even though for early life-time (t/D_0^2 = 0.1 s) the D_0 = 2.0 mm droplet features the highest soot reaction class rates, for t/D_0^2 = 0.5 s and D_0 = 2.0 mm only oxidation occurs, conversely for D_0 = 1.0 mm both inception and growth mechanisms dominates soot chemistry, while for D_0 = 0.6 mm at t/D_0^2 = 0.5 s soot oxidation already competes with soot growth. Finally, from Figs. 11b-d it is possible to observe the correspondence between the spatial location of the peak soot volume fraction, i.e. the

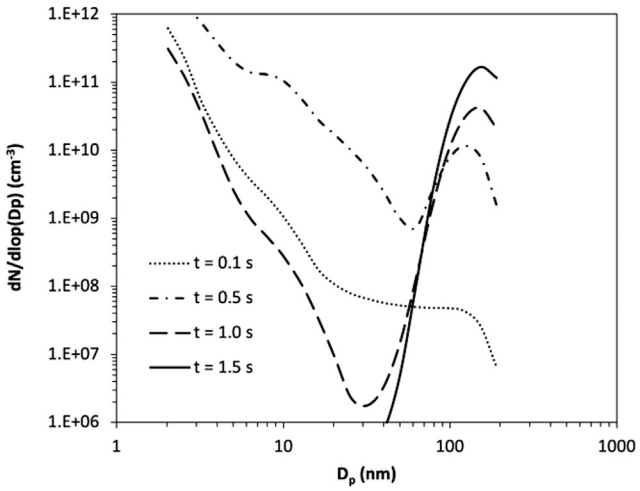

Fig. 9. Evolution over time of the soot particle size distribution in the n-heptane droplet of initial diameter of 1 mm on the soot shell (dashed line in Fig. 7b).

soot shell, and that of the zero net velocity closer to the droplet surface, which represents a stable equilibrium point for particles and aggregates, as discussed by Stagni et al. [11].

5. Conclusions

In this work we numerically investigated the formation of soot particles and aggregates in the combustion of spherically-symmetric, isolated fuel droplets of n-heptane. A 1D mathematical model, including detailed description of thermodynamics and transport properties of liquid and gaseous phase, radiative heat transfer, and detailed kinetics, was adopted. Soot formation and evolution was included via a Discrete Sectional Model, extensively validated in premixed and diffusion laminar flames, which accounts for the most relevant chemical and physical phenomena (nucleation, surface growth, coagulation, aggregation, and oxidation).

The mathematical model was adopted to explain the non-monotonic tendency to soot formation with the initial droplet diameter, experimentally reported for isolated large droplets ($D_0 = 0.5 - 3$ mm). The numerical simulations showed that the maximum of soot formation occurring for droplets with intermediate initial diameters is the result of the competition of two phenomena: on the one hand, the increase in droplet diameter tends to increase soot formation due to the longer lifetime of the droplet itself; on the other hand, however, larger diameters correspond to larger radiative losses, leading to a decrease in the flame temperature, which slows down soot formation reactions, leading to a decrease in soot.

Kinetic analysis highlighted the different evolution of large PAHs, spherical particles and aggregates varying initial droplet diameter. When the latter increases, spatial and temporal fields of soot and its precursors shrink. Specifically, after 0.5 s, the $D_0 = 0.5$ mm droplet is almost completely consumed, breaking off soot formation. Conversely, for $D_0 = 1.0$ mm, surface growth continues governing soot chemistry thanks to both the fuel availability and the still high gas-phase temperature, while for $D_0 = 2.0$ mm the low temperature due to the large radiative losses leads to soot consumption through oxidation, dominant over soot formation in such conditions.

The simulations also showed that the thermophoretic effect is responsible for the high volume fractions of soot (on the order of tens of ppm) observed experimentally and numerically in the combustion of isolated fuel droplets, which cannot be observed in more conventional combustion systems, such as premixed and diffusive flames. Moreover, the uniquely high residence times experienced by soot coming from

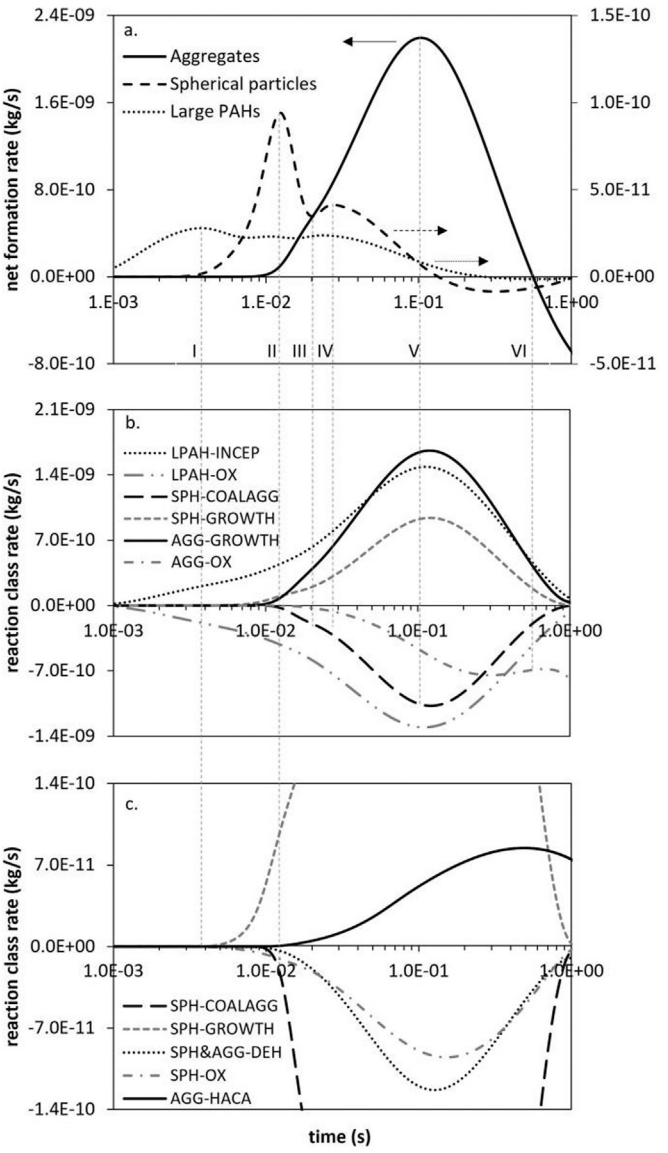

Fig. 10. Temporal evolution of: (a) the integral, net formation rates of large PAHs, soot spherical particles and aggregates for a n-heptane droplet of initial diameter of 1 mm and of (b,c) the rates of the main reaction classes considered in the soot model adopted.

large droplet combustion (of the order of seconds) result in the formation of unusually large aggregates (up to ~ 200 nm), making this type of system of interest for exploring soot formation in more unconventional conditions.

Even if the numerical results analyzed and discussed in the present work are able to capture reasonably well the experimental observations, the quantitative agreement is not equally satisfactory. There are several reasons which can explain the discrepancies observed in Fig. 1. As already pointed out, in addition to the inevitable uncertainties in experimental measurements, the physical and chemical complexity of the investigated system required simplifying assumptions and/or adoption of simplified models. Also based on previous works, the main limitation of the adopted numerical framework seems to be the radiative heat transfer model, based on the assumption of a gray gas. More advanced models, based on a spectral description of the gaseous phase (as adopted in [34] for example), are expected to improve the predictive capability of the framework, especially in the ability to capture the radiative extinction of large droplet with higher accuracy.

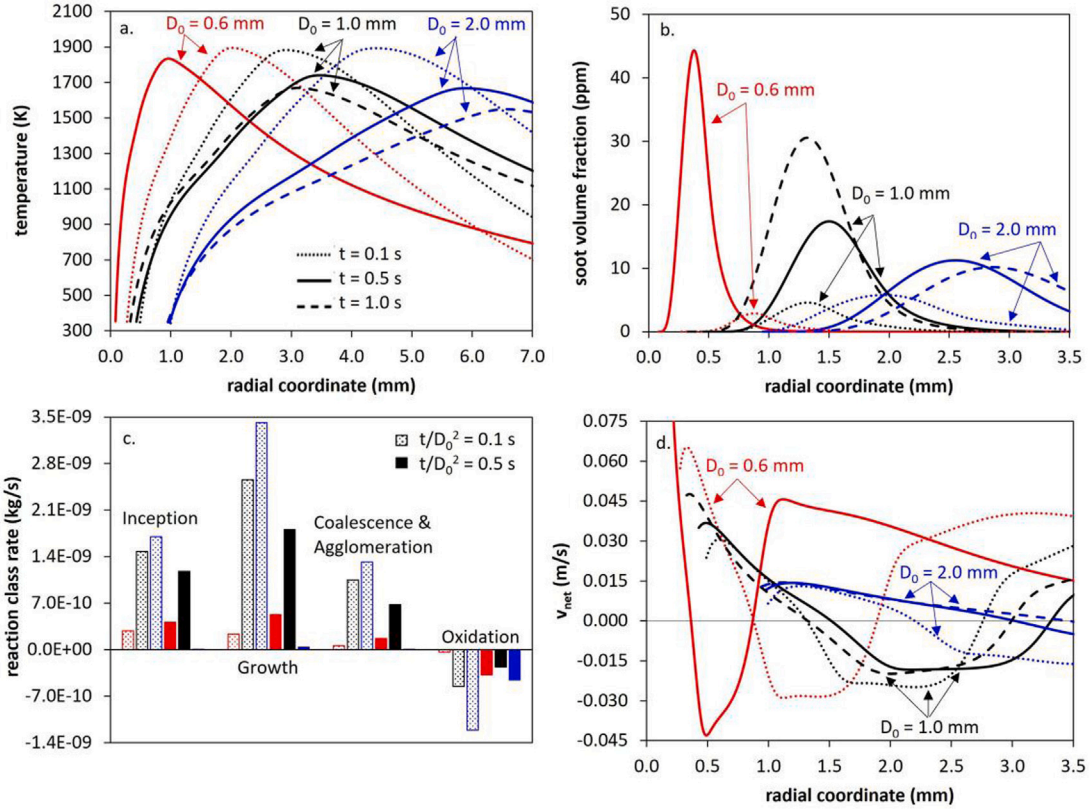

Fig. 11. Radial profiles of: (a) flame temperature T_f, (b) soot volume fraction fv_{max} for droplets with initial diameters of 0.6, 1.0 and 2.0 mm. (c) Radially integrated rates of the main soot reaction classes at different scaled times t/D_0^2. (d) Radial profiles of net velocity v_{net}. (For interpretation of the references to color in this figure legend, the reader is referred to the web version of this article).

Moreover, an additional complexity is represented by the soot model: to date, there is still no model for soot formation and evolution with proven predictive capabilities for complex fuels in a wide range of operating conditions. More specifically, the Discrete Sectional Model adopted in the present work is continuously updated and extended. Thus, the predictive capabilities of the whole framework are expected to improve in the next future, leading to a better agreement with the experimental data.

CRediT authorship contribution statement

Andrea Nobili: Writing – review & editing, Investigation, Formal analysis, Conceptualization. **Alessio Frassoldati:** Writing – review & editing, Methodology. **Tiziano Faravelli:** Methodology, Writing – review & editing. **Alberto Cuoci:** Conceptualization, Software, Supervision, Investigation, Writing – original draft.

Declaration of competing interest

The authors declare the following financial interests/personal relationships which may be considered as potential competing interests: Tiziano Faravelli reports financial support was provided by MIUR (Ministero dell'Istruzione e del Merito).

Data availability

No data was used for the research described in the article.

Acknowledgments

The authors gratefully acknowledge the financial support of MIUR with the PRIN 2017 MAGIC DUST (Modeling and Analysis of carbon nanoparticles for innovative applications Generated dIrectly and Collected DUring combuSTion) project (2017PJ5XXX).

Appendix A. Supplementary data

Supplementary material related to this article can be found online at https://doi.org/10.1016/j.fuel.2023.130403.

References

[1] Liu Y, Xu Y, Hicks M, Avedisian C. Comprehensive study of initial diameter effects and other observations on convection-free droplet combustion in the standard atmosphere for n-heptane, n-octane, and n-decane. Combust Flame 2016;171:27–41. http://dx.doi.org/10.1016/j.combustflame.2016.05.013.

[2] Kumagai S, Sakai T, Okajima S. Combustion of free fuel droplets in a freely falling chamber. Symp (Int) Combust 1971;13(1):779–85. http://dx.doi.org/10.1016/S0082-0784(71)80080-2, Thirteenth symposium (International) on Combustion.

[3] Okajima S, Kumagai S. Further investigations of combustion of free droplets in a freely falling chamber including moving droplets. Symp (Int) Combust 1975;15(1):401–7. http://dx.doi.org/10.1016/S0082-0784(75)80314-6.

[4] Shaw B, Dryer F, Williams F, Haggard J. Sooting and disruption in spherically symmetrical combustion of decane droplets in air. Acta Astronaut 1988;17(11–12):1195–202.

[5] Jackson G, Avedisian C, Yang J. Observations of soot during droplet combustion at low gravity: heptane and heptane/monochloroalkane mixtures. Int J Heat Mass Transfer 1992;35(8):2017–33. http://dx.doi.org/10.1016/0017-9310(92)90203-5.

[6] Urban BD, Kroenlein K, Kazakov A, Dryer FL, Yozgatligil A, Choi MY, et al. Sooting behavior of ethanol droplet combustion at elevated pressures under microgravity conditions. Microgravity Sci Technol 2004;15(3):12–8.

[7] Knight B, Williams FA. Observations on the burning of droplets in the absence of buoyancy. Combust Flame 1980;38:111–9. http://dx.doi.org/10.1016/0010-2180(80)90044-9.

[8] Mikami M, Niwa M, Kato H, Sato J, Kono M. Clarification of the flame structure of droplet burning based on temperature measurement in microgravity. Symp (Int) Combust 1994;25(1):439–46. http://dx.doi.org/10.1016/S0082-0784(06)80672-7.

[9] Choi MY, Lee K-O. Investigation of sooting in microgravity droplet combustion. In: Symposium (international) on combustion, vol. 26. Elsevier; 1996, p. 1243–9.

[10] Manzello SL, Choi MY, Kazakov A, Dryer FL, Dobashi R, Hirano T. The burning of large n-heptane droplets in microgravity. Proc Combust Inst 2000;28(1):1079–86.
[11] Stagni A, Cuoci A, Frassoldati A, Ranzi E, Faravelli T. Numerical investigation of soot formation from microgravity droplet combustion using heterogeneous chemistry. Combust Flame 2018;189:393–406. http://dx.doi.org/10.1016/j.combustflame.2017.10.029.
[12] Choi M, Yozgatligil A, Dryer F, Kazakov A, Ddbashi R. Experiments and model development for the investigation of sooting and radiation effects in microgravity droplet combustion. NASA internal report CP—2001-210826, 2001.
[13] Cuoci A, Mehl M, Buzzi-Ferraris G, Faravelli T, Manca D, Ranzi E. Autoignition and burning rates of fuel droplets under microgravity. Combust Flame 2005;143(3):211–26.
[14] Santachiara G, Prodi F, Cornetti C. Experimental measurements on thermophoresis in the transition region. J Aerosol Sci 2002;33(5):769–80.
[15] Viskanta R, Merriam RL. Heat transfer by combined conduction and radiation between concentric spheres separated by radiating medium. J Heat Transfer 1968;90(2):248–55. http://dx.doi.org/10.1115/1.3597493.
[16] Modest MF. Radiative heat transfer. Academic Press; 2013.
[17] Cuoci A, Saufi A, Frassoldati A, Dietrich D, Williams F, Faravelli T. Flame extinction and low-temperature combustion of isolated fuel droplets of n-alkanes. Proc Combust Inst 2017;36(2):2531–9. http://dx.doi.org/10.1016/j.proci.2016.08.019.
[18] Ascher UM, Petzold LR. Computer methods for ordinary differential equations and differential-algebraic equations. Philadelphia: SIAM; 1998.
[19] Buzzi-Ferraris G. Scientific C++: Building numerical libraries the object-oriented way. New York: Addison Wesley/Longman; 1993.
[20] Ferraris GB, Manca D. BzzOde: a new C++ class for the solution of stiff and non-stiff ordinary differential equation systems. Comput Chem Eng 1998;22(11):1595–621. http://dx.doi.org/10.1016/S0098-1354(98)00233-6.
[21] Ranzi E, Frassoldati A, Stagni A, Pelucchi M, Cuoci A, Faravelli T. Reduced kinetic schemes of complex reaction systems: Fossil and biomass-derived transportation fuels. Int J Chem Kinet 2014;46(9):512–42.
[22] Nobili A, Cuoci A, Pejpichestakul W, Pelucchi M, Cavallotti C, Faravelli T. Modeling soot particles as stable radicals: a chemical kinetic study on formation and oxidation. Part I. Soot formation in ethylene laminar premixed and counterflow diffusion flames. Combust Flame 2022;112073.
[23] Johansson K, Head-Gordon M, Schrader P, Wilson K, Michelsen H. Resonance-stabilized hydrocarbon-radical chain reactions may explain soot inception and growth. Science 2018;361(6406):997–1000.
[24] Commodo M, Kaiser K, De Falco G, Minutolo P, Schulz F, D'Anna A, et al. On the early stages of soot formation: Molecular structure elucidation by high-resolution atomic force microscopy. Combust Flame 2019;205:154–64.
[25] Nobili A, Maffei LP, Baggioli A, Pelucchi M, Cuoci A, Cavallotti C, et al. On the radical behavior of large polycyclic aromatic hydrocarbons in soot formation and oxidation. Combust Flame 2022;235:111692.
[26] Saggese C, Ferrario S, Camacho J, Cuoci A, Frassoldati A, Ranzi E, et al. Kinetic modeling of particle size distribution of soot in a premixed burner-stabilized stagnation ethylene flame. Combust Flame 2015;162(9):3356–69.
[27] Pejpichestakul W, Ranzi E, Pelucchi M, Frassoldati A, Cuoci A, Parente A, et al. Examination of a soot model in premixed laminar flames at fuel-rich conditions. Proc Combust Inst 2019;37(1):1013–21. http://dx.doi.org/10.1016/j.proci.2018.06.104.
[28] Sirignano WA. Fluid dynamics and transport of droplets and sprays. Cambridge University Press; 2010.
[29] Cuoci A, Avedisian CT, Brunson JD, Guo S, Dalili A, Wang Y, et al. Simulating combustion of a seven-component surrogate for a gasoline/ethanol blend including soot formation and comparison with experiments. Fuel 2021;288:119451. http://dx.doi.org/10.1016/j.fuel.2020.119451.
[30] Nayagam V, Dietrich D, Hicks M, Williams F. Cool-flame extinction during n-alkane droplet combustion in microgravity. Combust Flame 2015;162(5):2140–7. http://dx.doi.org/10.1016/j.combustflame.2015.01.012.
[31] Wang H. Formation of nascent soot and other condensed-phase materials in flames. Proc Combust Inst 2011;33(1):41–67.
[32] Singh J, Patterson RI, Kraft M, Wang H. Numerical simulation and sensitivity analysis of detailed soot particle size distribution in laminar premixed ethylene flames. Combust Flame 2006;145(1):117–27.
[33] Camacho J, Tao Y, Wang H. Kinetics of nascent soot oxidation by molecular oxygen in a flow reactor. Proc Combust Inst 2015;35(2):1887–94.
[34] Farouk T, Dryer F. Isolated n-heptane droplet combustion in microgravity: "Cool Flames" - Two-stage combustion. Combust Flame 2014;161(2):565–81. http://dx.doi.org/10.1016/j.combustflame.2013.09.011.